

## SPARKLING EUV BRIGHT DOTS OBSERVED WITH HI-C

S. RÉGNIER<sup>1</sup>, C. E. ALEXANDER<sup>1</sup>, R. W. WALSH<sup>1</sup>, A. R. WINEBARGER<sup>2</sup>, J. CIRTAİN<sup>2</sup>, L. GOLUB<sup>3</sup>, K. E. KORRECK<sup>3</sup>, N. MITCHELL<sup>4</sup>, S. PLATT<sup>4</sup>, M. WEBER<sup>3</sup>, B. DE PONTIEU<sup>5</sup>, A. TITLE<sup>5</sup>, K. KOBAYASHI<sup>6</sup>, S. KUZIN<sup>7</sup>, AND C. E. DEFOREST<sup>8</sup>

*Draft version December 9, 2019*

### ABSTRACT

Observing the Sun at high time and spatial scales is a step towards understanding the finest and fundamental scales of heating events in the solar corona. The Hi-C instrument has provided the highest spatial and temporal resolution images of the solar corona in the EUV wavelength range to date. Hi-C observed an active region on 11 July 2012, which exhibits several interesting features in the EUV line at 193Å: one of them is the existence of short, small brightenings “sparkling” at the edge of the active region; we call these EUV Bright Dots (EBDs). Individual EBDs have a characteristic duration of 25s with a characteristic length of 680 km. These brightenings are not fully resolved by the SDO/AIA instrument at the same wavelength, however, they can be identified with respect to the Hi-C location of the EBDs. In addition, EBDs are seen in other chromospheric/coronal channels of SDO/AIA suggesting a temperature between 0.5 and 1.5 MK. Based on their frequency in the Hi-C time series, we define four different categories of EBDs: single peak, double peak, long duration, and bursty EBDs. Based on a potential field extrapolation from an SDO/HMI magnetogram, the EBDs appear at the footpoints of large-scale trans-equatorial coronal loops. The Hi-C observations provide the first evidence of small-scale EUV heating events at the base of these coronal loops, which have a free magnetic energy of the order of  $10^{26}$  erg.

*Subject headings:* Sun:UV radiation — Sun: magnetic fields — Sun: corona — Sun: activity

### 1. INTRODUCTION

A long standing problem in solar physics is how the solar corona is heated up to a temperature of few million degrees while the photosphere is at about 6000 K. Several models have been developed either to heat the coronal plasma locally or to transport heat from the lower layers of the solar atmosphere into the corona (see for instance review by Klimchuk 2006), however, these models often lack an explanation for an average temperature of 1MK for the entire corona and its sustainability during a solar cycle. This strongly suggests that several mechanisms may be at play, each of them providing a substantial amount of heat to the corona and, which can vary during the activity cycle of the Sun. Those models also invoke smaller spatial and time scales than the ones provided by the current observations.

So, the critical issue is really to answer the questions: where is the source of heat located? and where and how does the heating take place? Along a given magnetic structure (often a coronal loop), three scenarios are often considered: the release of energy is located (i) at the footpoints of the structure in the photospheric layer which

is the most favorable location owed to the importance of the photospheric motions and the source of material and energy transported from the convection zone, (ii) at the apex of the structure, and (iii) uniformly along the structure. Those three scenarios imply that the heat is transported along the magnetic structures, and that we actually observe loop-like structures in the corona. In terms of observations, it has been difficult to disentangle the actual location of the heat source. As an example, several authors using a dataset obtained in soft X-rays by *Yohkoh*/SXT have reached an opposite conclusion depending on how they dealt with the data reduction (Mackay et al. 2000; Priest et al. 2000; Reale 2002). To determine the possible heating scenario, the authors looked at the profile of temperature along the coronal loop and compared with a theoretical model. These indirect methods were needed because of the coarse spatial and time resolutions of *Yohkoh*/SXT (compared to what can be achieved nowadays). In this paper, with the development of new high spatial and time resolution instrumentation, we are looking for a direct evidence of the source of heat deposition, observationally characterized by a small, short increase in intensity.

Theoretically, the different heating locations (apex, uniform or footpoint) arise from the idea that magnetic energy stored in the chromosphere/corona produces small, short bursts converting the magnetic energy into thermal and/or kinetic energy (rapidly converted into heat). This is the basic principle of Parker’s theory (1988) for heating the solar corona by nanoflares. A large number of those small events is needed to sustain and uniformly distribute the heat in the entire solar corona. The mechanism responsible for the release of magnetic energy could be, for instance, magnetic reconnection, wave mode coupling or turbulence. As a large amount of the free energy contained in the magnetic field structure

<sup>1</sup> Jeremiah Horrocks Institute, University of Central Lancashire, Preston, Lancashire, PR1 2HE, UK

<sup>2</sup> NASA Marshall Space Flight Center, VP 62, Huntsville, AL 35812, USA

<sup>3</sup> Harvard-Smithsonian Center for Astrophysics, 60 Garden Street, Cambridge, MA 02138, USA

<sup>4</sup> School of Computing, Engineering and Physical Sciences, University of Central Lancashire, Preston, Lancashire, PR1 2HE, UK

<sup>5</sup> Lockheed Martin Solar and Astrophysics Laboratory, 3251 Hanover Street, Palo Alto, CA 94304, USA

<sup>6</sup> Center for Space Plasma and Aeronomic Research, 320 Sparkman Dr, Huntsville, AL 35805, USA

<sup>7</sup> Lebedev Physical Institute, Russian Academy of Sciences, Leninskii pr. 53, Moscow, 119991 Russia

<sup>8</sup> Southwest Research Institute, 1050 Walnut Street Suite 300, Boulder, CO 80302, USA

of active regions is located at the base of the corona or in the chromosphere (R gnier and Priest 2007), the most favorable heating location is at the footpoints of coronal loops. For the quiet Sun, the footpoints of the coronal structures are the most effected by the photospheric motions such as granular motions which can easily produce tangled/braided/twisted magnetic flux bundles. In this paper, we combine EUV observations and a magnetic field model to determine if Parker’s model is a viable scenario, even if we cannot identify the mechanism(s) responsible for the energy release.

High-resolution ground-based instruments in the visible-wavelength domain allowed to observe new structures and phenomena in the lower layers of the solar atmosphere, especially small-scale brightenings or events such as spicules or Ellerman bombs (see e.g., Scharmer 2003; Berger et al. 2004; Rutten et al. 2004; Rouppe van der Voort et al. 2005; Beck et al. 2007). In conjunction, the investigation of the coronal plasma at EUV wavelengths is in constant improvement in terms of spatial and temporal resolution. For instance, the Atmospheric Imager Assembly (AIA; Lemen et al. 2012) on board the Solar Dynamics Observatory (SDO; Pesnell, Thompson and Chamberlin 2012) is largely contributing to a new era of fast (12s) small-scale (pixel size of  $0.6''$ ) observations of the solar corona always discovering new phenomena. As a new step forward, the Hi-C instrument has provided high-temporal (5.5s) and high-spatial (pixel size of  $0.1''$ ) resolution observations of the EUV corona. Using this dataset, Cirtain et al. (2013) have recently shown the existence of small-scale braided structures within the active region, and evidenced the magnetic reconnection process occurring within the braided structures. In addition, two recent articles relying on Hi-C data have provided new insights in the existence of small-scale heating events. Testa et al. (2013) have found that the active region moss is highly dynamic with a variability on timescales of 15s, and the moss brightenings lead to an energy release of  $10^{23}$  erg (order of magnitude consistent with the nanoflare model). Similarly, Winebarger et al. (2013) have investigated transient brightenings along small-scale transition-region loops. It was found that the loops have a diameter ranging from  $0.9''$  to  $1.1''$  with an average duration of 64s. Winebarger et al. (2013) have estimated that these brightenings radiate an energy of about  $10^{24}$ – $10^{25}$  erg again an energy estimate consistent with the nanoflare model.

In this paper, we report on the existence of an additional heat source for the coronal plasma: EUV, short-lived (25 s), small-scale ( $<1''$ ) brightenings taking place in the low layers of the solar atmosphere ( $\log T = 5.5$ – $6.5$ ). We call these brightenings EUV bright dots (EBDs). This new discovery is made possible by the high spatial resolution and fast time cadence of the Hi-C data.

In Section 2, after introducing the Hi-C instrument, we characterize the location, size, and thermal properties of EBDs as derived from the Hi-C channel and six SDO/AIA channels. We thus study their time evolution in the observed region (Section 3), as well as their magnetic properties (Section 4) relying on a potential field extrapolation of one SDO/HMI magnetogram. In Section 2.4, the possible temperature of EBDs is inves-

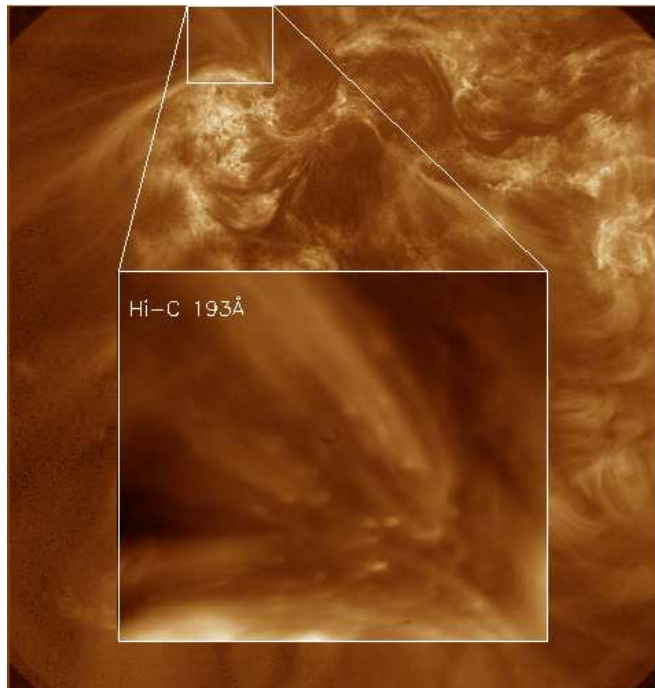


FIG. 1.— Location of the region of interest containing the EBDs in the Hi-C FOV recorded at 18:53:32 UT on 11 July 2012.

tigated using the EM loci method. The conclusions are drawn in Section 5.

## 2. STRUCTURE OF EUV BRIGHT DOTS

### 2.1. The Hi-C Instrument

The High-resolution Coronal (Hi-C) imager was launched on a sounding rocket on July 11, 2012 (Kobayashi et al. 2013). The Hi-C passband isolates a very narrow window in EUV centered at  $193 \text{ \AA}$ , taking images with a pixel size of  $0.1''$ . The intensity line profile is dominated by an emission line of Fe XII with a peak temperature at 1.5 MK ( $\log T = 6.17$ ), and blended by some weak transition region lines, as well as including 10-15 MK emission during large flares. The main target of the Hi-C instrument was the complex system of active regions located around the central meridian in the Southern hemisphere (active regions NOAA 11519-21), and which indeed mostly contains the active region 11520 (AR11520). In Fig. 1, we plot the full Hi-C field-of-view (FOV) centered approximately at  $[-150, -281]$  arcseconds from the Sun center. We extract the region of interest containing the EBDs discussed in this paper. The size of the EBDs FOV is of approximately  $35'' \times 30''$ . Magnetically, AR11520 is a collection of 7-8 sunspots as can be seen in Fig. 10 left. The Hi-C time series lasts during 200 s from 18:52:09 UT to 18:55:29 UT with a time cadence of 5.5 s (36 images).

### 2.2. Comparing Hi-C and SDO/AIA Observations

In Fig. 2, we compare the EUV emission at  $193 \text{ \AA}$  observed in Hi-C (left) and SDO/AIA (right, Lemen et al. 2012). Even if centered on the same wavelength, the Hi-C and SDO/AIA filters are similar but not identical. The high spatial resolution of the Hi-C observations provides further insights into the small-scale coro-

nal structures/phenomena observed as localized brightenings; EBDs that can be resolved in the Hi-C FOV are seen as compact bright regions in the SDO/AIA FOV. To extract the signature of the EBDs, we proceed in three consecutive steps: (i) applying a median filter to a single frame, (ii) considering the intensities above the  $3\sigma$ -level (standard deviation of the intensity map in a single frame), and (iii) adding the intensities of the frames together over the whole Hi-C time series. We thus can define the locations of significant bright dots (see Fig. 2 bottom left), and subsequently study their time evolution and geometrical properties. Here, eight significant bright dots are identified (as depicted by the rectangles in Fig. 2 bottom left). The eight different EBDs have been chosen as they are associated with a well-defined structure in individual images: elliptical structures of more than 9 pixels and with an intensity above the  $3\sigma$ -level (standard deviation of a single frame). Even if they do not obey the criteria imposed above, other brightenings (not classified as EBDs) exist in the FOV, which suggest that smaller spatial-scale structures can exist.

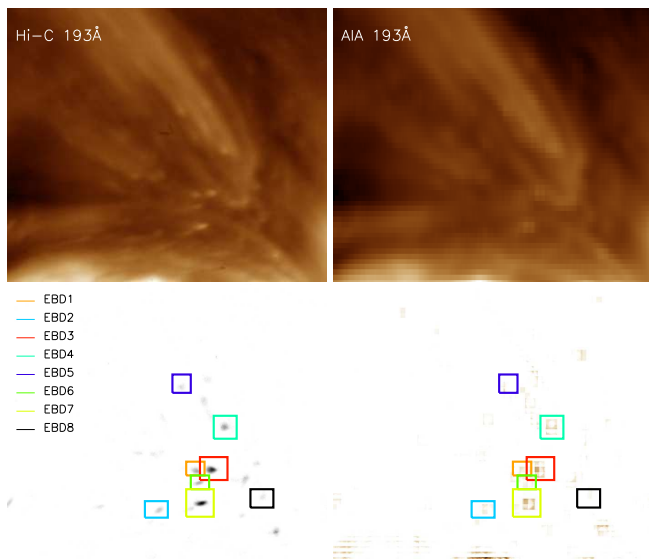


FIG. 2.— Top row: integrated intensities over the whole Hi-C time series observed in Hi-C at 193 Å (left), and in SDO/AIA at 193 Å (right); Bottom row: filtered and integrated intensities during the whole Hi-C time series: (left) Hi-C EBDs, (right) SDO/AIA EBDs.

In Fig. 2 bottom right, the location of the EBDs selected in the Hi-C image (left) is compared to the SDO/AIA image (right) processed with the same methodology as the Hi-C data: most of the chosen EBDs can be identified in both fields-of-view. Solely based on the images, the signal is much weaker for the SDO/AIA observations, and thus using SDO/AIA observations alone would not provide confidence of their existence; only the comparison with the Hi-C images ensures that the SDO/AIA EBDs are true brightenings and not just noise.

### 2.3. Multi-wavelength Observations of EBDs

Using the capabilities of the SDO/AIA instrument, we study the EBDs using six other wavelength channels covering from the low chromosphere to the high temperature

corona (1600Å, 304Å, 131Å, 171Å, 211Å, and 335Å). In Fig. 3 top, we plot the integrated images over the whole Hi-C time series in the different channels for the same FOV. In Fig. 3 bottom, we apply the same data analysis procedure to the time series for the six wavelength channels in order to enhance the location of EBDs.

From Fig. 3, we find the following possible signatures of EBDs:

- the 1600Å channel does not show much evidence of EBD intensity signature.
- the 304Å channel shows a weak emission for some of the EBDs.
- the hotter channels (131Å, 171Å, 211Å, and 335Å) show a clear evidence of EBD intensity signatures as in the 193Å channel.

Comparing the temperature response functions of SDO/AIA and their overlapping areas (Boerner et al. 2012), this multi-channel analysis suggests that the EBDs are in a temperature range between 0.3 to 1.5 MK ( $\log(T) = 5.5 - 6.2$ ) which implies that the EBDs are located at the top of the chromosphere or at the bottom of the corona.

### 2.4. EBD's Temperature: EM Loci

In order to investigate the possible temperature of the EBDs, the EM loci technique was employed: the same method as in Alexander et al. (2013) was used, especially to get the temperature response functions of the different SDO/AIA and Hi-C channels. The EM loci method (e. g., Jordan et al. 1987; del Zanna et al. 2002) allows us to determine if a coronal structure is isothermal or multi-thermal without providing more in-depth information (see Fig. 7 in Reale 2010 for an example of isothermal and multi-thermal loops). We derived the EM loci curves of several SDO/AIA channels (131Å, 171Å, 193Å, 211Å, 335Å) and the 193Å Hi-C channel. A single crossing of all the EM loci curves should indicated an isothermal plasma at this temperature.

In Fig. 4, we present the results of the EM loci method for EBD3: there is a clear evidence that three possible temperature regions corresponding to the larger number of loci crossings may be distinguished: one at low temperature at  $\log(T) = 5.5$ , and two at coronal temperature with  $\log(T) = 6.0$  and  $\log(T) = 6.4$ . However, for all the other EBDs studied, the EM loci method does not lead to any conclusive temperature, the crossings being distributed between  $\log(T) = 5.3 - 6.5$ . The lack of clarity in the EM loci curves maybe the result of two points: either (i) the size and timing of the EBD's structure at the SDO/AIA scale do not permit to draw any firm conclusions (as noted in Section 2, the EBDs are very difficult to observe in SDO/AIA data), or (ii) the plasma of the EBDs is a transition region plasma for which a temperature cannot be determined by the lines observed. The latter will imply that the mechanism to release magnetic energy most likely occurs at the foot-points of the coronal loops. The behavior of the EM loci method for the EBDs as observed by SDO/AIA is consistent with the study of multi-thermal plasma performed by Guennou et al. (2012).

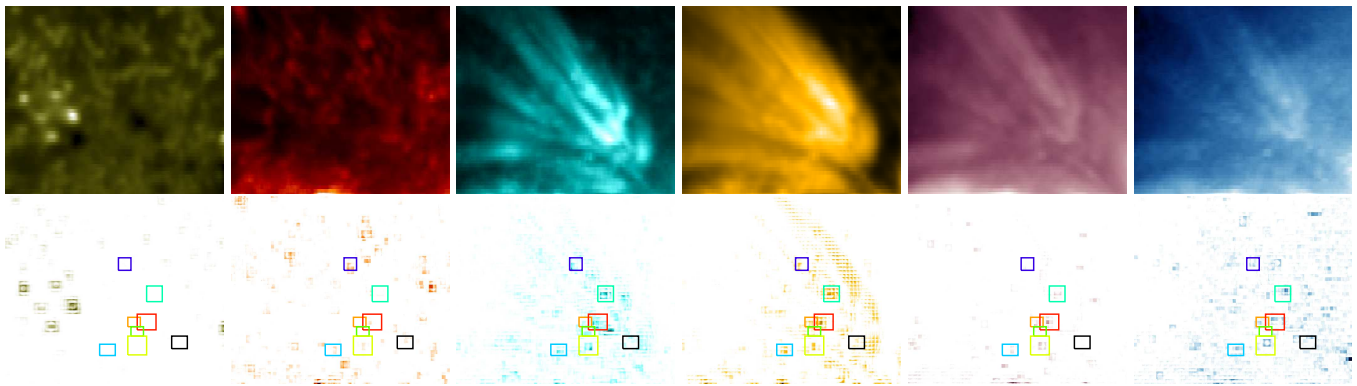


FIG. 3.— (Top) Integrated intensity SDO/AIA images at 1600 Å, 304 Å, 131 Å, 171 Å, 211 Å, 335 Å (from left to right) in the same FOV and at the nearest time to the Hi-C image in Fig. 2. (Bottom) filtered images as in Fig. 2 bottom (some color coding as in Fig. 2).

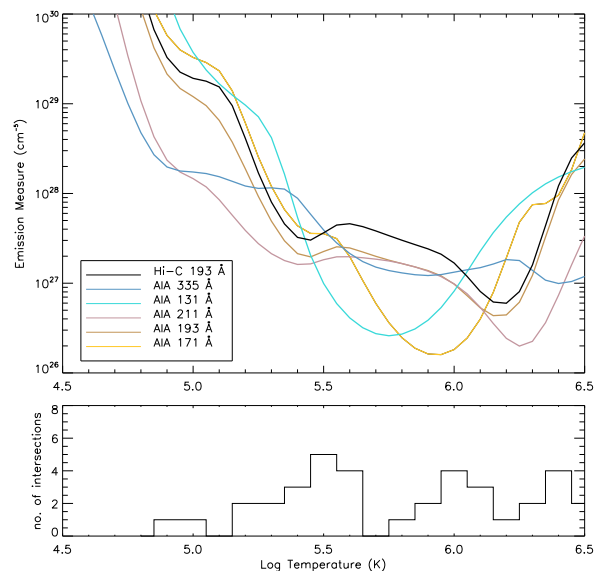


FIG. 4.— EM loci for EBD3 at the peak of intensity. (Top) EM loci curves for the different SDO/AIA channels and Hi-C intensity. (Bottom) Number of crossing at a given temperature bin.

### 3. CHARACTERISTICS AND DYNAMICS OF EBDS

#### 3.1. EBD's Categories

We analyse the Hi-C light curves and images of the eight selected EBDS within the areas depicted in Fig. 2 bottom left. In Table 1, we give the main observed characteristics for the eight chosen EBDS including the time of the peak intensity  $t_{peak}$ , the relative intensity  $\Delta I$  of the maximum intensity at  $t_{peak}$  with respect to the average intensity over the full EBD FOV at the same time, the duration  $\Delta_{peak}$  from the light curve given by the width at half-maximum of the intensity peak (with respect to the minimum intensity of the light curve), and  $\Delta_v$  the time during which a coherent structure (elliptical surface of intensity covering more than 9 pixels) can be identified within the time series, and the characteristic length (major axis of the ellipse) of the EBDS. The area considered for individual EBDS is the size of the rectangle depicted in Fig. 2 bottom left.

TABLE 1  
CHARACTERISTIC PARAMETERS OF EBDS

	Cat.	Name	Peak time $t_{peak}$ (UT)	$\Delta I$	Duration (s) $\Delta_{peak}$	$\Delta_v$	Length (Mm)
Single	I	EBD1	18:52:48	1.68	27	64	0.65
		EBD2	18:52:59	2.00	39	61	0.5
		EBD3	18:54:06	3.89	22	89	0.86
	Average values			2.52	29s	71s	0.67 Mm
Double-peak	II	EBD4	18:52:59	1.99	28	61	0.43
			18:53:16	1.82	22		0.76
		EBD5	18:53:10	1.55	23	56	0.76
			18:53:43	1.52	28		0.72
	EBD6	18:54:56	1.76	16	83	0.65	
	18:55:12	1.84	22		0.76		
Average values			1.75	23s	67s	0.68 Mm	
Long Duration	III	EBD7	18:52:31	1.34	23	200	D
			18:52:59	1.70	23		0.43
			18:53:43	1.98	28		0.79
			18:54:17	2.06	23		0.79
			18:54:45	1.93	5		0.57
			18:55:01	2.38	16		0.79
Average values			1.89	20s	200s	0.67 Mm	
Bursty	IV	EBD8	18:53:21	1.28	5	133	0.43
			18:53:43	1.32	5		0.43
			18:54:00	1.47	5		0.43
			18:54:45	1.44	5		0.43
			18:54:56	1.44	5		0.43
Average values			1.39	5s	133s	0.43 Mm	

From Table 1, we deduce that, in average, EBDS have a characteristic life-time of 25s, a characteristic length of 0.68 Mm.

From the light curves of the identified EBDS, we distinguish four categories of EBDS based on their frequency within the Hi-C time series (see Figs 5–8 top, and also Table 1):

**I. Single Peak** single events with a clear peak in the

light curve. EBD1–3 have a duration between 22 and 39s, and a characteristic size between 0.5 and 0.86 Mm;

**II. Double Peak** double-peaked EBDs with two consecutive maxima. EBD4–6 have two peaks separated by 17–33s, and with a short global duration (about 67s);

**III. Long Duration** long-duration EBDs for which the coherent structure can be characterized during the entire time series (200s), and with several distinct maxima. For EBD7, six intensity peaks are observed within the Hi-C time series with a time interval from 16s to 44s. In Table 1, the value "D" means that the EBD intensity distribution is diffuse;

**IV. Bursty** a series of very short brightenings related to a coherent structure, and leading to an increase of the overall intensity. EBD8 light curve shows an increase of intensity starting at 18:53:16 UT, and has several short peaks (5s) observed with a cadence from 11s to 45s.

From this small sample of events, Categories I and II are the most significant. We now proceed to a detailed analysis of one single EBD in each of the four categories. For Categories I and II, the EBD analysed has the largest intensity contrast ( $\Delta I$  in Table 1).

### 3.2. Category I: Single Peak

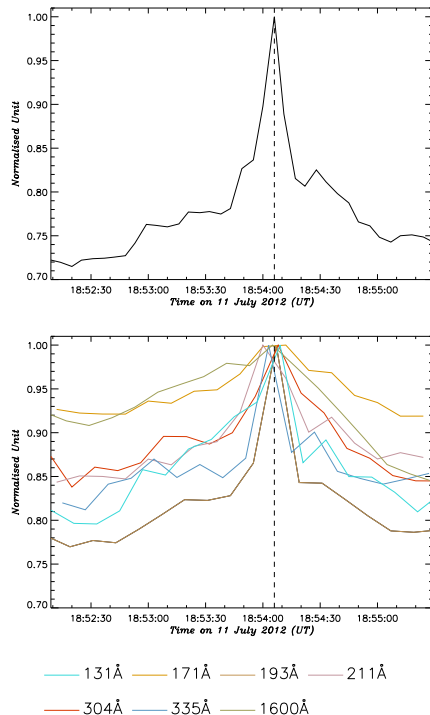


FIG. 5.— (Top) Hi-C normalised light curve for EBD3 showing clearly the single peak of intensity characterising the bright dot. (Bottom) SDO/AIA normalised light curves for the same area encompassing EBD3 in seven different EUV-UV channels (131Å, 171Å, 193Å, 211Å, 304Å, 335Å, and 1600Å)

Consider EBD3; in Fig. 5 top, we plot the Hi-C normalised light curve of EBD3, which exhibits a clearly distinctive peak in intensity. The peak lasts during 5 frames (22 s). We also plot the normalised light curves for different SDO/AIA channels (see Fig. 5 bottom) where we distinguish a corresponding peak in intensity (see Fig. 9a). Due to the short duration of the EBDs ( $\sim 22$ s) and the time cadence of SDO/AIA images (12s), it is difficult to conclude when the peak emission has actually occurred in the different channel. As shown by Viall and Klimchuk (2011, 2012), the cooling of a nanoflare storm within a coronal loop may be deduced from the ordering of the appearance of intensity peaks in the SDO/AIA light curves. This result follows the observational work done by Winebarger et al. (2003) using TRACE data. Such analysis cannot be performed here.

### 3.3. Category II: Double Peak

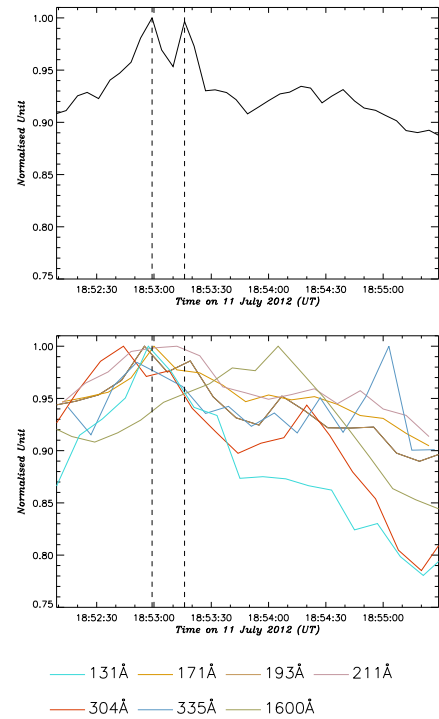


FIG. 6.— Same as Fig. 5 for EBD4 in Category II

In Fig. 6 top, the normalised Hi-C light curve for EBD4 clearly shows two distinct consecutive peaks (see Fig. 9b): each individual peak has the property of the EBDs of Category I. In Fig. 6 bottom, the peaks are also observed in the 193Å and 171Å SDO/AIA channels. The first peak at 18:52:59 UT is clearly observed in the other channels, while the second peak cannot be identified.

### 3.4. Category III: Long Duration

In Fig. 7, we plot the Hi-C normalised light curve (top) and the SDO/AIA light curves (bottom) for EBD7, the only example of Category III EBDs. The Hi-C light curve shows several intensity peaks that can be observed during the whole time period. The peaks (marked by vertical dashed lines) appear at 18:52:31 UT, 18:52:59 UT,

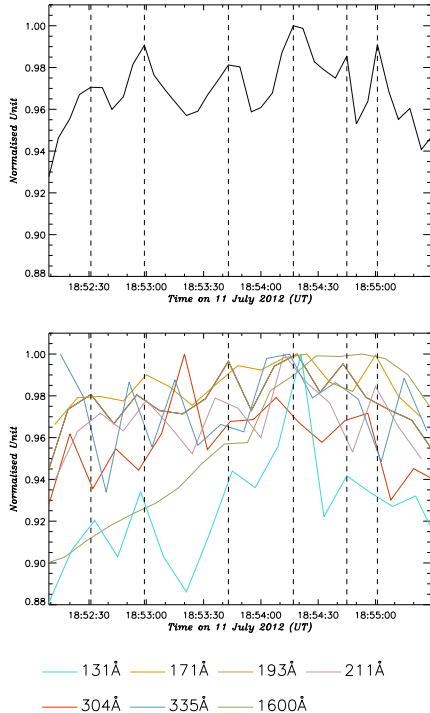


FIG. 7.— Same as Fig. 5 for EBD7 in Category III

18:53:43 UT, 18:54:17 UT, 18:54:45 UT, and 18:55:01 UT. These Hi-C peaks are also observed in the 193Å SDO/AIA channel with a comparable mean intensity value, and most of them can be seen in the 131Å, 171Å. We also notice that the normalised light curves of 211Å, 304Å and 335Å exhibit a similar bursty behavior but at different time. EBD7 is observed as a coherent structure during the whole Hi-C time series (see Fig. 9c). It is also possible to observe a slight displacement of the center-of-mass of EBD7, which leads to an apparent transverse velocity of  $4.2 \text{ km s}^{-1}$  for a duration of 106s. The EBDs recur at a period of about 30s.

### 3.5. Category IV: Bursty

In Fig. 8, we see a clear increase in intensity from 18:53:16 UT to the end of the Hi-C time series: several peaks are observed during this period. The identified peaks appear at 18:53:21 UT, 18:53:43 UT, 18:54:00 UT, 18:54:45 UT, and 18:54:56 UT (see also Fig. 9d). The peaks are not all seen in the 193Å SDO/AIA channel due to their short duration and the time span between consecutive SDO/AIA images. The EBDs recur at a period of about 20s. This short period and the increase of intensity suggest that the energy released during the EBDs heats up the plasma without the possibility for the conductive cooling to take place.

## 4. MAGNETIC FIELD STRUCTURE

### 4.1. SDO/HMI Data and Extrapolated Magnetic Field Over Hi-C FOV

A line-of-sight magnetogram provided by SDO/HMI (Scherrer et al. 2012) allows us to extrapolate the potential magnetic field into the solar atmosphere. The

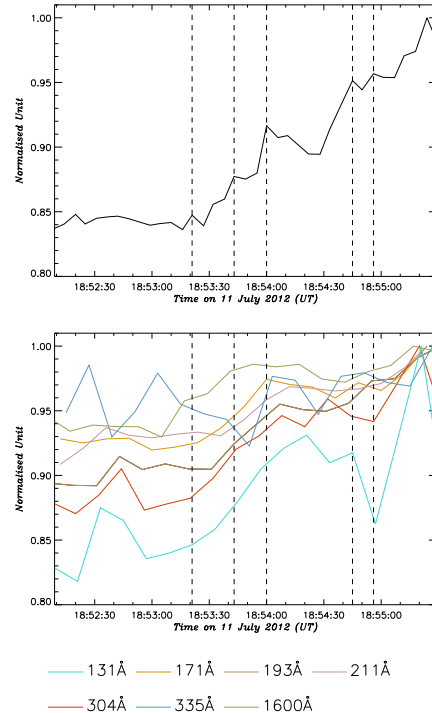


FIG. 8.— Same as Fig. 5 for EBD8 in Category IV

SDO/HMI magnetogram has been captured on July 11, 2012 at 18:54:00 UT with a pixel size of  $0.5''$ .

The potential field assumption considers that

$$\vec{\nabla} \times \vec{B} = \vec{0}. \quad (1)$$

The system of differential equations is solved as a boundary value problem in defining the normal component of the magnetic field on each surface of the computational box. Two types of potential fields are computed; (i) the potential field for which the original SDO/HMI magnetogram (see Fig. 10 left) is used as bottom boundary condition, and open boundary conditions on the sides and top of the computational box are applied, (ii) the fully open potential field within the computational box (as defined by Aly 1984) for which the magnetic field at the bottom boundary is unipolar. The first extrapolated magnetic field corresponds to a minimum of magnetic energy for this set of normal magnetic field distributions, whilst the second model corresponds to an upper bound of magnetic energy for a force-free field (Aly 1984). Thus the difference between the magnetic energies derived from both models gives an upper bound for the free magnetic energy contained in the magnetic configuration.

In Fig. 10 left, the selected SDO/HMI FOV can be seen ( $144 \times 126 \text{ Mm}^2$ ), which includes most of AR11520 and for which the total unsigned magnetic flux is nearly balanced (see Table 2). In Fig. 10 right, we plot the Hi-C FOV corresponding to the location of the EBDs. Subsequently, in Table 2, we summarize the magnetic properties of the full FOV used to perform the potential field extrapolation, and then reduced to the EBD FOV:

- the minimum and maximum line-of-sight magnetic field strength for the photospheric magnetogram

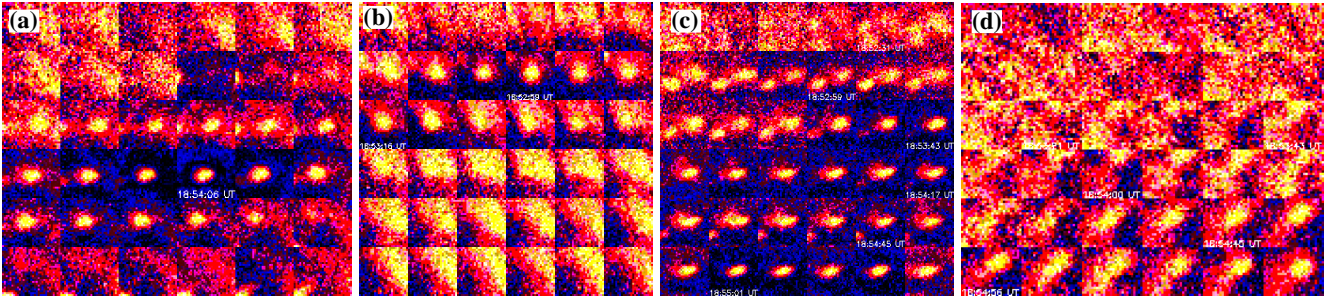


FIG. 9.— Time evolution of the intensity associated with the four EBDs studied: (a) EBD3 (FOV:  $3.1'' \times 2.6''$ ), (b) EBD4 (FOV:  $2.6'' \times 2.6''$ ), (c) EBD7 (FOV:  $3.1'' \times 3.1''$ ), and (d) EBD8 (FOV:  $2.6'' \times 2.1''$ ). Time increases from left to right, and top to bottom. The time of the peaks marked on the light curves is annotated on the images. The images have been normalised to the maximum EBD intensity in the Hi-C time series.

( $B_{los}^{min}$ ,  $B_{los}^{max}$  respectively);

- the total unsigned magnetic flux ( $\phi_T$ ),

$$\phi_T = \int_S |B_z| dS \quad (2)$$

where  $S$  is the photospheric surface;

- the net magnetic flux ( $\phi_{net}$ ),

$$\phi_{net} = \int_S B_z dS; \quad (3)$$

- the positive and negative magnetic fluxes ( $\phi_+$ ,  $\phi_-$  respectively):

$$\phi_+ = \int_{\Omega^+} B_z dS \quad \phi_- = \int_{\Omega^-} B_z dS \quad (4)$$

where  $\Omega^+$  and  $\Omega^-$  are the domains of positive (resp. negative)  $B_z$  on the photospheric surface;

- the magnetic energy derived from the potential magnetic field with open boundary conditions ( $E_{pot}$ ) and from the fully open magnetic field ( $E_{open}$ ). By definition, the magnetic energy  $E_m$  for a magnetic field vector  $B$  is given by

$$E_m = \int_V \frac{B^2}{2\mu_0} dV \quad (5)$$

where  $V$  is the volume of the computational box and  $\mu_0$  is the vacuum permeability.

Note that the full FOV has a total unsigned magnetic flux through the photosphere almost balanced, while the magnetic flux for the EBD FOV is dominated by the negative flux. As can be seen in Fig. 11, the histogram of the line-of-sight magnetic field strength in the EBD area shows that the negative polarity is dominant in this area and is (almost) unipolar. However, it is worth noting that the negative polarity where the EBDs are observed is not located in a sunspot (concentrated intense unipolar magnetic field) but more like in a plage magnetic field region (diffuse magnetic field which can contain parasitic polarities), so we cannot rule out the presence of small-scale positive polarities, which cannot be resolved by SDO/HMI and which can play an important role in terms of low-lying magnetic reconnection events.

In Fig. 12, we plot a selection of magnetic field lines, which describes the global magnetic geometry of

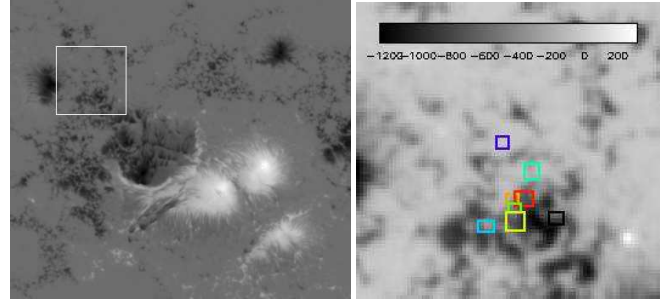


FIG. 10.— (Left) Line-of-sight magnetic field distribution in the full Hi-C FOV observed by SDO/HMI. The EBD FOV is indicated by the white rectangle; (Right) close-up of the magnetic field in the area where the EBDs are observed (same color coding as in Fig. 2 bottom). The line-of-sight magnetic field strength (G) is indicated by the color bar.

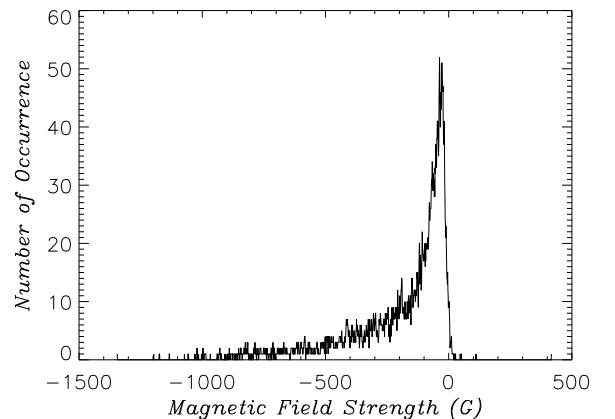


FIG. 11.— Histogram of the line-of-sight magnetic field strength in the region depicted in Fig. 10 right.

AR11520 derived from a potential field approximation. Fig. 12 highlights the magnetic connectivity between the sunspots of AR11520 and outside (West side) towards AR11519 and AR11521. We also plot a significant amount of magnetic field lines in and near the area containing the EBDs: this shows that those magnetic field lines are open (i.e., leaving the computational box) towards the East and North sides. It is worth noting that the magnetic field lines oriented towards the North are associated with transequatorial loops connecting to the

TABLE 2  
MAGNETIC PROPERTIES

	$B_{los}^{min}$ (G)	$B_{los}^{max}$ (G)	$\phi_T$ (Mx)	$\phi_{net}$ (Mx)	$\phi_+$ (Mx)	$\phi_-$ (Mx)	$E_{pot}$ (erg)	$E_{open}$ (erg)
Full FOV	-1830	2463	$5.97 \times 10^{22}$	$-9.00 \times 10^{21}$	$2.53 \times 10^{22}$	$-3.43 \times 10^{22}$	$1.68 \times 10^{33}$	$3.03 \times 10^{33}$
EBD FOV	-1232	316	$2.61 \times 10^{21}$	$-2.60 \times 10^{21}$	$7.43 \times 10^{18}$	$-2.60 \times 10^{21}$	$5.20 \times 10^{31}$	$8.98 \times 10^{31}$

positive polarity of a diffuse, decaying active region in the Northern hemisphere.

Table 2 displays the magnetic energy of the potential and open magnetic field configuration for both the full FOV and EBD FOV. The magnetic energy of the full FOV is typical for an active region with a photospheric flux of the order of  $10^{22}$  Mx. The upper bound for the free magnetic energy is estimated to be  $E_{open} - E_{pot} = 1.35 \times 10^{33}$  erg, consistent with the high-level of activity in AR11520 for a couple of days around the Hi-C observations (including an X1.4 flare on 12 July 2012). The upper bound for the free magnetic energy in the EBD FOV is estimated to  $3.78 \times 10^{31}$  erg. Therefore, energy-release events such as nanoflare (with an energy of  $10^{24}$  erg) can be generated within the EBD FOV.

#### 4.2. EBD's Magnetic Field Structure

We now study the magnetic properties of individual EBDs considering the same four events as in the Section 3. For the sake of clarity, in Fig. 13, we only plot a selection of magnetic field lines associated with EBD3 (Cat I), EBD4 (Cat II), EBD7 (Cat III), and EBD8 (Cat IV). For these EBDs, the magnetic field lines are leaving the computation box towards the North-East consistent with the observed transequatorial loops connecting two active regions (see Section 4.1). We extract the magnetic information for each set of magnetic field lines: it is above 1 Mm that the magnetic field strength becomes a smoothly, decaying function of height. Below 1 Mm, the magnetic field strength is influenced by the complexity of the magnetic field and the change in orientation of the transverse component (parallel to the photosphere). It is also below 1 Mm that the magnetic field lines plotted in Fig. 13 can be considered as radial. The magnetic field strength of the four EBDs below 1 Mm varies between 200 G and 280 G.

We estimate the magnetic energy associated with the EBDs by considering the potential field within a sphere of diameter 0.68 Mm (characteristic size of EBDs) and within 1Mm above the photosphere where the magnetic field strength has been estimated between 200 and 280 G. The magnetic energy is thus between  $1.98 \times 10^{26}$  and  $3.87 \times 10^{26}$  erg. An upper bound for the free magnetic energy is about 80% of the previous values, i.e.,  $1.58 - 3.1 \times 10^{26}$  erg.

The free magnetic energy estimates are of  $10^{26}$  erg which are similar to the energy associated with a single micro-flare. Thus the magnetic field associated with the EBDs contains enough free magnetic energy to power single or multiple nanoflares as envisioned by Parker (1988), knowing that a small part of the free magnetic energy is commonly released during flares (e.g., Amari et al. 2000). By invoking an energy release site reduced by a factor of 3 (0.23 Mm instead of 0.68 Mm), the magnetic energy

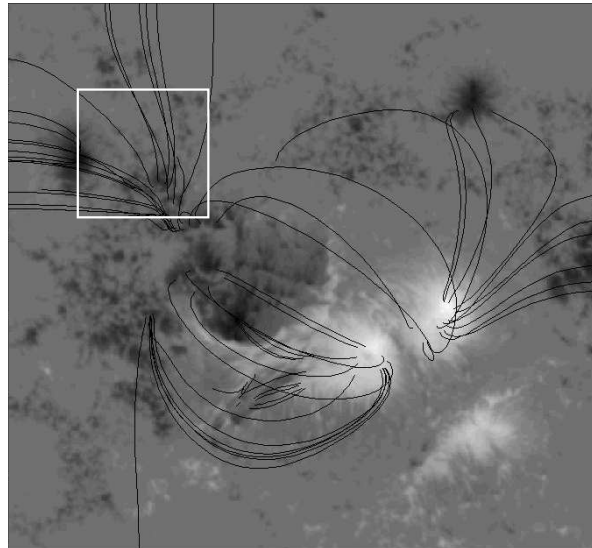


FIG. 12.— Selection of magnetic field lines within AR11520 extracted from the potential field extrapolation. The background image is the line-of-sight magnetic field observed by SDO/HMI. The white box indicates the field-of-view containing the EBDs as in Fig. 10.

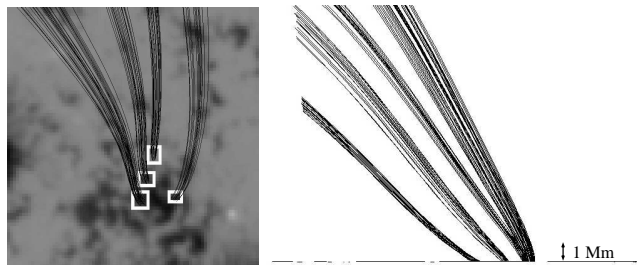


FIG. 13.— A selection of magnetic field lines for the four EBDs studied in Section 4.2. (Left) top view with the EBD's location depicted by white rectangles (see Fig. 2); (Right) view from the East side (North is on the left-hand side)

estimated reaches the nanoflare scale. This magnetic energy estimate evidences that the nanoflare model can be a viable mechanism to release magnetic energy at low-heights in the solar atmosphere and thus heat the coronal part of the loop.

## 5. CONCLUSIONS

The high resolution images obtained in the EUV by Hi-C allow us to determine the smallest brightenings observed to date in an active region in extreme ultra-violet light, called EUV bright dots (EBDs). These EBDs sparkle at the footpoints of large-scale coronal loops. We have grouped the EBDs into four categories depending on their recurrence. Except for the fourth category



(successive, short-lived EBDs), individual EBDs which can be extracted from the Hi-C time series have the same characteristic duration (about 25s) and length scale (0.68 Mm). Using a potential field extrapolation of the SDO/HMI line-of-sight photospheric magnetic field, we have determined that the EBDs observed in the Hi-C FOV are located at the footpoints of large-scale magnetic loops connecting the active regions 11520 to a decaying active region in the Northern hemisphere. The above properties suggest that EBDs might be a signature of an impulsive release of energy located at the base of coronal loops.

In terms of energetics, the magnetic energy estimate is of the order of  $10^{26}$  erg which is 100 times more than required by the nanoflare model suggested by Parker (1988). However, our estimate is an upper bound for the free magnetic energy than can be released, thus suggesting that smaller scale structures can exist. Nevertheless, Testa et al. (2013) and Winebarger et al. (2013) have estimated the radiated energy to  $10^{24}$  erg, which is compatible with the order of magnitude of the magnetic energy: according to Emslie et al. (2012) who performed a complete study of the energy partition in eruptive events, the magnetic energy budget can be two orders of magnitude larger than the radiated energy.

Even if it is not possible to compare quantitatively due to the lack of spectroscopic data overlying the Hi-C FOV, it is important to mention the observations of Hara (2009), which showed that small-scale brightenings at the footpoints of coronal loops can be observed with a strong redshift velocity close to the local sound speed. Hara (2009) suggested that spatially unresolved ( $<720$  km) structures could exist at the footpoint of coronal loops.

According to Walsh, Bell and Hood (1995), the conduction time-scale can be expressed as  $\tau_c = pL^2/\kappa_0 T^{7/2}$

where  $p$  is the plasma pressure,  $L$  the characteristic length,  $\kappa_0$  the thermal conductivity in the corona ( $\kappa_0 = 10^{-11}$ ), and  $T$  is the temperature. The characteristic length  $L$  of the loop is chosen to be the loop length along which the heating is assumed to take place:  $L = 5$  Mm. For a plasma pressure of  $0.1 \text{ dyne}\cdot\text{cm}^{-2}$  and a temperature range from 0.5 to 1.5 MK, the conductive time-scale is between 6 s at 1.5 MK and 5 min at 0.5 MK. A characteristic time of 25 s gives a characteristic temperature of 1 MK. Thus, the observed life-time of EBDs maybe compatible with the properties of a coronal plasma.

With the restricted observations of the Hi-C instrument (short flight and limited FOV), questions arise for further study of these elementary events: how often/common are EBDs in active regions? Are they always located at the footpoints of long coronal loops? What is their contribution towards the global heating of the corona? Can EBDs be associated with Type 2 spicules or even Ellerman bombs, both having similar time scales? Several of these questions can be addressed by finding criteria which will enable the detection of EBDs in SDO/AIA images going forward, and by using high resolution chromospheric spectroscopic observations from IRIS.

We thank Jonathan Cirtain and Amy Winebarger for their help and discussion on the Hi-C instrument and to improve this manuscript. MSFC/NASA led the mission and partners include the Smithsonian Astrophysical Observatory in Cambridge, Mass.; Lockheed Martin's Solar Astrophysical Laboratory in Palo Alto, Calif.; the University of Central Lancashire in Lancashire, England; and the Lebedev Physical Institute of the Russian Academy of Sciences in Moscow.

## REFERENCES

- Alexander, C. E., Walsh, R. W., Régnier, S., et al. 2013, *ApJ*, 775, L32
- Aly, J. J. 1984, *ApJ*, 283, 349
- Amari, T., Luciani, J. F., Mikic, Z., Linker, J. 2000, *ApJ*, 529, L49
- Beck, C., Bellot Rubio, L. R., Schlichenmaier, R., Sütterlin, P. 2007, *A&A*, 472, 607
- Berger, T. E., Rouppe van der Voort, L. H. M., Löfdahl, M. G., Carlsson, M., Fossum, A., Hansteen, V. H., Marthinussen, E., Title, A., Scharmer, G. 2004, *A&A*, 428, 613
- Boerner, P., Edwards, C., Lemen, J., Rausch, A., Schrijver, C., Shine, R., Shing, L., Stern, R., Tarbell, T., Title, A., Wolfson, C. J., Soufi, R., Spiller, E., Gullikson, E., McKenzie, D., Windt, D., Golub, L., Podgorski, W., Testa, P., Weber, M. 2012, *Sol. Phys.*, 275, 41
- Cirtain, J. W., Golub, L., Winebarger, A. R., DePontieu, B., Kobayashi, K., Moore, R. L., Walsh, R. W., Korreck, K. E., McCauley, P., Title, A., Kuzin, S., DeForest, C. E. 2013, *Nature*, 493, 501
- del Zanna, G., Landini, M., Mason, H. E. 2002, 385, 968
- Emslie, A. G., Dennis, B. R., Shih, A. Y., Chamberlin, P. C., Mewaldt, R. A., Moore, C. S., Share, G. H., Vourlidas, A., Welsch, B. T. 2012, *ApJ*, 759, 71
- Guennou, C., Auchère, F., Soubrié, E., Bocchialini, K., Parenti, S., Barbey, N. 2012, *ApJS*, 203, 26
- Hara, H. 2009, in *The Second Hinode Science Meeting: Beyond Discovery-Toward Understanding*, ASPC, eds. Lites, B., Cheung, M., Magara, T., Mariska, J., Reeves, K., 415, 252
- Jordan, C., Ayres, T. R., Brown, A., Linsky, J. L., Simon, T. 1987, *MNRAS*, 225, 903
- Klimchuk, J. A. 2006, *Sol. Phys.*, 234, 41
- Kobayashi, K., Cirtain, J., Winebarger, A. R., Korreck, K. E., Golub, L., Walsh, R. W., De Pontieu, B., DeForest, C. E., Title, A., Kuzin, S., Savage, S., Beabout, D., Beabout, B., Podgorski, W., Caldwell, D., McCracken, K., Ordway, M., Bergner, H., Gates, R., McKillop, S., Cheimets, P., Platt, S., Mitchell, N., Windt, D. 2013, submitted to *Sol. Phys.*
- Lemen, J. R., Title, A. M., Akin, D. J., Boerner, P. F., Chou, C., et al. 2012, *Sol. Phys.*, 275, 17
- Mackay, D. H., Galsgaard, K., Priest, E. R., Foley, C. R. 2000, *Sol. Phys.*, 193, 93
- O'Dwyer, B., Del Zanna, G., Mason, H. E., Weber, M. A., Tripathi, D. 2010, *A&A*, 521, 21
- Parker, E. N. 1988, *ApJ*, 330, 474
- Pesnell, W. D. and Thompson, B. J. and Chamberlin, P. C. 2012, *Sol. Phys.*, 275, 3
- Priest, E. R., Foley, C. R., Heyvaerts, J., Arber, T. D., Mackay, D., Culhane, J. L., Acton, L. W. 2000, *ApJ*, 539, 1002
- Reale, F. 2002, *ApJ*, 580, 566
- Reale, F. 2010, *Living Reviews in Solar Physics*, 7, 5
- Régnier, S. and Priest, E. R. 2007, *A&A*, 468, 701
- Rouppe van der Voort, L. H. M., Hansteen, V. H., Carlsson, M., Fossum, A., Marthinussen, E., van Noort, M. J., Berger, T. E. 2005, *A&A*, 435, 327
- Rutten, R. J., Hammerschlag, R. H., Bettonvil, F. C. M., Sütterlin, P., de Wijn, A. G. 2004, *A&A*, 413, 1183
- Scharmer, G. B. and Bjelksjo, K. and Korhonen, T. K. and Lindberg, B. and Petterson, B. 2003, *Society of Photo-Optical Instrumentation Engineers (SPIE) Conference Series*, eds Keil, S. L. and Avakyan, S. V., 4853, 341
- Scherrer, P. H., Schou, J., Bush, R. I., Kosovichev, A. G., Bogart, R. S., Hoeksema, J. T., Liu, Y., Duvall, T. L., Zhao, J., Title, A. M., Schrijver, C. J., Tarbell, T. D., Tomczyk, S. 2012, *Sol. Phys.*, 275, 207

- Testa, P., De Pontieu, B., Martínez-Sykora, J., DeLuca, E., Hansteen, V., Cirtain, J., Winebarger, A., Golub, L., Kobayashi, K., Korreck, K., Kuzin, S., Walsh, R., DeForest, C., Title, A., Weber, M. 2013, ApJ, 770, L1
- Viall, N. M. and Klimchuk, J. A. 2011, ApJ, 738, 24
- Viall, N. M. and Klimchuk, J. A. 2012, ApJ, 753, 35
- Walsh, R. W., Bell, G. E., Hood, A. W. 1995, Sol. Phys., 161, 83
- Winebarger, A. R., Walsh, R. W., Moore, R., De Pontieu, B., Hansteen, V., Cirtain, J., Golub, L., Kobayashi, K., Korreck, K., DeForest, C., Weber, M., Title, A., Kuzin, S. 2013, ApJ, 771, 21
- Winebarger, A. R., Warren, H. P., Seaton, D. B. 2003, ApJ, 593, 1164